ACS NANO

www.acsnano.org

ARTICLE

Identifying and Visualizing the Edge Terminations of Single-Layer $MoSe_2$ Island Epitaxially Grown on Au(111)

Jianchen Lu,[†] De-Liang Bao,[†] Kai Qian, Shuai Zhang, Hui Chen, Xiao Lin,* Shi-Xuan Du,* and Hong-Jun Gao

Institute of Physics & University of Chinese Academy of Sciences, Chinese Academy of Sciences, Beijing 100190, P. R. China

Supporting Information

ABSTRACT: **Recently, single-layer transition-metal dichalcogenides have drawn significant attention due to their remarkable physical properties in the monolayer as well as at the edges. Here, we constructed high-quality, single-layer $MoSe_2$ islands on the Au(111) surfaces in ultrahigh vacuum by molecular beam epitaxy. All of the islands have hexagonal or triangular shapes with two kinds of well-defined edges. Scanning tunneling spectroscopy (STS) curves show notable differences in positive sample bias for the two types of edges. Density functional theory calculations for several edge configurations of $MoSe_2$ confirm that the STS differences are attributed to the coupling between the p_z orbital of Se atoms and the d_{xz} orbital of Mo atoms, and the two types of observed edge terminations are the bare Se edge and selenium-saturated Mo edge.**

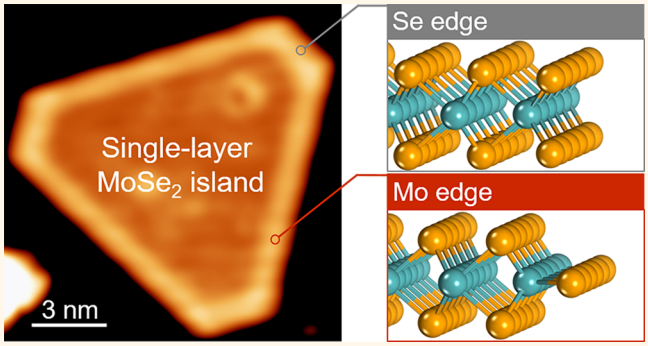

KEYWORDS: *single-layer $MoSe_2$ islands, edge terminations, scanning tunneling microscopy, scanning tunneling spectroscopy, density functional theory, molecular beam epitaxy*

Single-layer transition-metal dichalcogenides (TMDCs) are attracting tremendous interest due to their narrow bandgap, indirect-to-direct band gap transition,[1−4] strong spin−orbit coupling, and valley-related physics, making them attractive for a wide range of applications from electronics and optoelectronics to spin and valleytronic devices.[2,5−7] Among the more than 40 types of compounds in the TMDC family, MoS_2 and $MoSe_2$ are the most extensively studied. Compared to MoS_2, $MoSe_2$ has a narrower direct bandgap of ∼1.5 eV, which is close to the optimal bandgap value for single-junction solar cells and photoelectrochemical cells,[8,9] and it has a larger spin-splitting energy of ∼180 meV at the top of its valence bands, making it more applicable than MoS_2 in spintronics.[10,11] Meanwhile, in contrast to the bulk material, single-layer TMDCs have been shown to have lots of intriguing properties. Three examples are a direct bandgap that results in different optical properties,[4,12] a conduction band minimum at the K point of the Brillouin zone that indicates the possibilities for valley and spin-valley physics,[7,13,14] and enhanced Coulomb interactions that lead to giant bandgap renormalization and excitonic effects in the molecular beam epitaxial (MBE) growth of single-layer $MoSe_2$.[10,15]

The findings of edge investigations of two-dimensional (2D) materials play an essential role in practical applications, such as the magnetic order on zigzag edges of graphene nanoribbons.[16] The edge configurations and edge states of TMDC materials have drawn much attention for their enhancement of activity in the hydrodesulfurization,[17] oxygen reduction reactions,[18] and hydrogen evolution reactions (HER).[19,20] Most studies show that the edge states are responsible for this enhanced activity[21−23] because of the inertness and insulation of the basal plane of TMDCs. However, to the best of our knowledge, an investigation of the edge terminations and edge states of single-layer $MoSe_2$ is currently lacking.

In the present work, we report successful epitaxial growth of high-quality single-layer $MoSe_2$ islands with two types of edge terminations on Au(111) surfaces. The atomic structure of the $MoSe_2$ islands was determined by a combination of density functional theory (DFT) calculations and scanning tunneling microscopy (STM). Raman characterizations demonstrate the single-layer nature of the $MoSe_2$. Core-level XPS spectra show a

Received: November 7, 2016
Accepted: February 11, 2017
Published: February 11, 2017

DOI: 10.1021/acsnano.6b07512
ACS Nano 2017, 11, 1689−1695

Mo^{4+} oxidation state and a Se^{2-} reduction state in the $MoSe_2$ film. Scanning tunneling spectroscopy (STS) investigations reveal an electronic bandgap of 1.86 eV in the basal plane of the $MoSe_2$ islands and a difference of electronic states between the two kinds of edges in one hexagonal $MoSe_2$ island. By performing DFT calculations, we determined that the single-layer $MoSe_2$ islands are terminated by bare Se edges alternating with selenium monomers saturated Mo edges. Furthermore, the difference of electronic states between the two types of edges is attributed to the coupling between the p_z orbital of Se atoms and the d_{xz} orbital of Mo atoms in the $MoSe_2$ edge.

RESULTS AND DISCUSSION

Figure 1a is a typical STM image of single-layer $MoSe_2$ islands on the Au(111) substrate with coverage of ~0.2 ML after one growth cycle, as described in the Methods. The individual $MoSe_2$ islands are clearly identified by well-defined hexagonal or triangular edges, which are similar to the MoS_2 islands on Au(111).[24,25] The side lengths vary from a few nanometers to more than 20 nanometers, and the line profile of an island (Figure S1c) shows that the height of the island is about 2.3 Å. Due to excessive selenium deposition, which is needed to prevent formation of the alloy Mo−Au, besides the regular $MoSe_2$ islands on the substrate, atoms also exist as small features on the Au(111) surface, as indicated by the white arrows in Figure 1a (see Figure S1a for clearer STM images). However, for single-layer MoS_2 nanoclusters on the Au(111) substrate, synthesized from Mo and H_2S, no such small features were observed due to the desorption of H_2S from the Au surface at temperatures above 160 K.[26,27] Moreover, in the control experiment, we deposited only Se atoms onto the Au(111) surface and obtained similar small features (Figure S1b). Therefore, we think these small features are Se atomic chains and triangular islands with a distance of 5.0 ± 0.05 Å between two Se atoms.

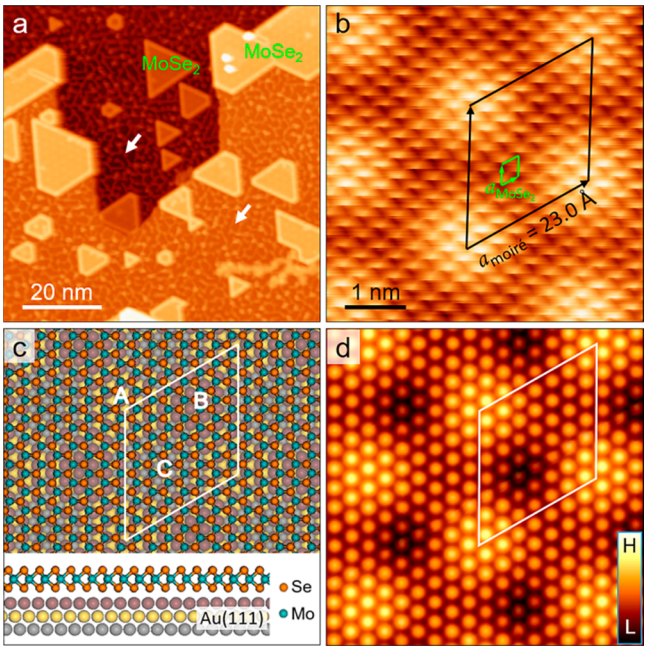

Figure 1. Atomic structure characterization of the as-grown single-layer $MoSe_2$ islands on Au(111) substrate. (a) STM image of single-layer $MoSe_2$ islands on Au(111) substrate ($MoSe_2$ coverage is ~0.2 ML). White arrows indicate excess Se species on Au(111) substrate. (b) Atomic-resolved STM image of single-layer $MoSe_2$ with hexagonal lattice. The light green and black rhombuses denote the unit cells of $MoSe_2$ lattice and the superstructure (moiré pattern), respectively. (c) Top view and side view of DFT optimized single-layer $MoSe_2$ atomic model on Au(111) surface. The white rhombus indicates the unit cell of the moiré pattern. Three domains in one unit cell are marked by A, B and C. (d) Theoretical simulated STM image based on the calculated structure in (c). Scanning parameters: (a) V_s = −1 V, I_t = 0.03 nA; (b) V_s = −0.5 V, I_t = 0.9 nA.

Large-size, single-layer $MoSe_2$ islands with ~0.7 ML (Figure S2a) were obtained after several growth cycles. A close-up STM image (Figure 1b) shows atomically resolved single-layer $MoSe_2$ with moiré superstructures. The high-resolution image presents a triangular arrangement of small protrusions with the lattice constant of a_{MoSe2} = 3.29 Å ± 0.05 Å (the unit cell is highlighted by the light green rhombus), which agrees perfectly with the previously reported value for single-layer $MoSe_2$.[15] Considering the structure of semiconductive 2*H*-$MoSe_2$, the small protrusions in Figure 1b should correspond to the topmost Se atoms of the $MoSe_2$ sheet. Moreover, we observed a larger periodic moiré superlattice (the black rhombus marks the unit cell), arising from the ~14% lattice mismatch between the $MoSe_2$ and Au(111). Obviously, the orientations of the moiré superlattice are aligned with those of the $MoSe_2$ lattice, and the lattice constant of the moiré superstructure is $a_{moiré}$ = 23.0 Å ± 0.1 Å, which is close to 7 times a_{MoSe2} and 8 times a_{Au}. Therefore, the moiré pattern can be explained as the (7 × 7) $MoSe_2$ supercells commensurately located on the (8 × 8) Au(111), *i.e.*, $a_{moiré}$ (23.0 Å) = 7 × a_{MoSe2} (3.29 Å) = 8 × a_{Au} (2.88 Å).

To obtain a detailed understanding of the atomic and electronic structures of the single-layer $MoSe_2$ on Au(111), we conducted density functional theory (DFT) calculations. Figure 1c shows the optimized atomic structure of $MoSe_2$/Au(111). In the top view (upper panel), we find that the orientations of the $MoSe_2$ layer are aligned with both Au(111) substrate and moiré superstructures, which agrees well with the experimental results. Obviously, it has three principal stacking domains (A, B, and C) in one unit cell of moiré superlattices (marked by white rhombus). In the side view (lower panel), we find that the height variation of single-layer $MoSe_2$ on Au substrate is 6.1 Å, which is much higher than the experimental observation (2.3 Å). The main reason is the semiconductor nature of $MoSe_2$ *versus* the metal nature of the Au substrate. Figure 1d shows the corresponding simulated STM image, demonstrating the periodic fluctuation of the moiré pattern. Those features are in good agreement with the experimental STM image in Figure 1b.

To further confirm the structural information and epitaxial relation, 2D fast Fourier transform (FFT) and low energy electron diffraction (LEED) of $MoSe_2$/Au(111) samples were carried out. Figure S2c is an FFT image obtained through an atomic-resolution STM image of $MoSe_2$ in Figure S2b. Clearly, the orientation of the moiré superstructure is aligned with the $MoSe_2$ lattice, as indicated by the black and blue arrows. In addition, a typical LEED pattern was obtained for the whole 10 mm diameter $MoSe_2$/Au(111) sample, as shown in Figure 2a. The outermost six diffraction spots (marked by the orange arrow) are assigned to the Au(111) substrate, and the inner six spots (marked by the blue arrow) with surrounding satellites (indicated by white arrow) are related to the $MoSe_2$ lattice and the moiré pattern, respectively. These sharp and clear

DOI: 10.1021/acsnano.6b07512
ACS Nano 2017, 11, 1689−1695

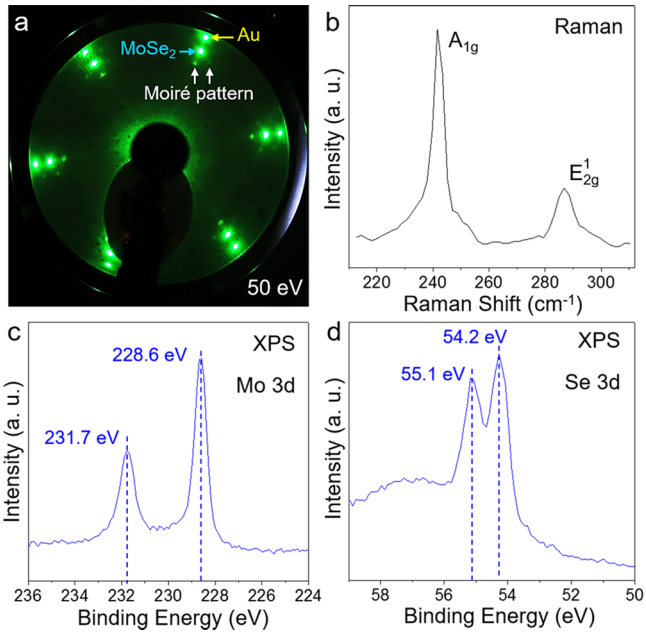

Figure 2. LEED, Raman scattering and core-level XPS spectra characterizations. (a) Typical LEED pattern of $MoSe_2$ film on Au(111) substrate. The yellow and blue arrows indicate the diffraction spots from the Au(111) lattice and $MoSe_2$ film, respectively. The other spots surrounding the diffraction spots of $MoSe_2$ result from the moiré superstructure, as indicated by the white arrows. (b) Raman spectrum of $MoSe_2$ film showing two characteristic peaks of single-layer $MoSe_2$ at 287.0 cm^{-1} (E_{2g}^1) and 241.8 cm^{-1} (A_{1g}). (c, d) XPS data of Mo 3d and Se 3d in $MoSe_2$/Au(111) sample, showing Mo $3d_{3/2}$ and $3d_{5/2}$ peaks at positions of 231.7 and 228.6 eV and Se $3d_{3/2}$ and $3d_{5/2}$ peaks at positions of 55.1 and 54.2 eV, respectively.

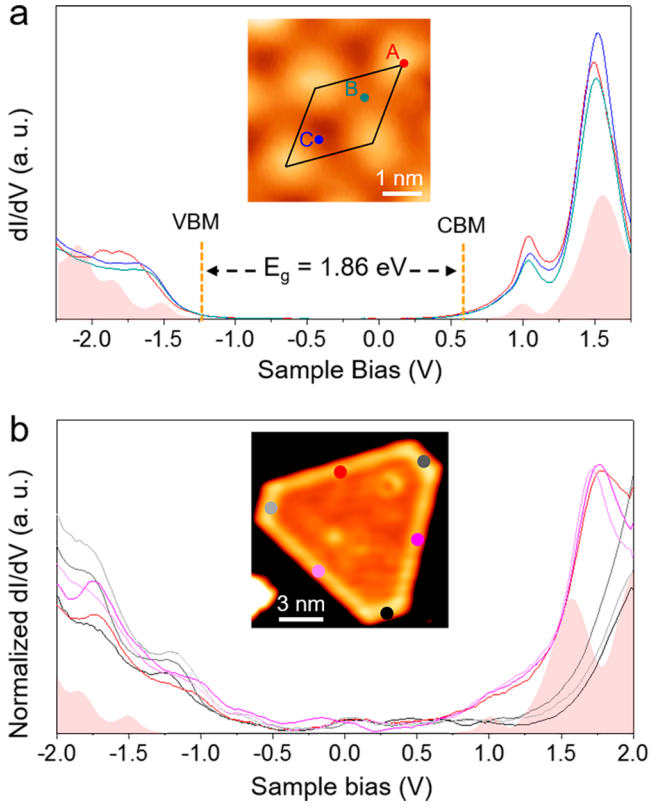

Figure 3. Electronic properties of single-layer $MoSe_2$ islands. (a) Normalized dI/dV curves obtained on the three different domains of single-layer $MoSe_2$ on Au(111), which are indicated by colored dots in the inset STM image. (b) Six normalized dI/dV curves taken on the six edges of one $MoSe_2$ island (inset STM image). The curves are obviously classified into two groups (black and red). The pink covered region in (a) and (b) are the DFT calculated density of state (DOS) of the single-layer $MoSe_2$. Scanning parameters: (a) V_s = −0.38 V, I_t = 0.1 nA, (b) V_s = −1.4 V, I_t = 0.1 nA.

diffraction spots mean a uniform and high quality $MoSe_2$ film has been successfully fabricated.

In order to assess the quality of the as-synthesized $MoSe_2$ film on Au(111), we carried out Raman characterization. Figure 2b is a typical Raman spectrum of $MoSe_2$/Au(111). Two characteristic Raman modes are clearly identified, A_{1g} mode (out-of-plane vibration) and E_{2g}^1 mode (in-plane vibration). The E_{2g}^1 mode located at 287.0 cm^{-1} is significantly lower in intensity than the A_{1g} mode located at 241.8 cm^{-1}. These positions and intensity of Raman modes confirm the presence of single-layer, high-quality $MoSe_2$ film on Au(111).[8,29,30] X-ray photoelectron spectroscopy measurements were performed to study the chemical compositions for the $MoSe_2$/Au(111) sample. Figure 2c,d shows the characteristic core level spectra of Mo and Se, respectively. The spectrum of Mo 3d electrons has two distinct peaks located at 231.7 and 228.6 eV, corresponding to the Mo $3d_{3/2}$ and $3d_{5/2}$ peaks, respectively, confirming that the molybdenum atoms in the $MoSe_2$ film are in the Mo(+4) state.[28] The Se 3d spectrum is identified as 55.1 eV (and 54.2 eV) of Se $3d_{3/2}$ (and $3d_{5/2}$) peaks, revealing the −2 oxidation chemical state of Se atoms in the single-layer $MoSe_2$/Au(111) sample.

The electronic properties of single-layer $MoSe_2$ on Au(111) surfaces were studied by STS. Figure 3a shows three normalized dI/dV spectra acquired on the center of three distinct domains of $MoSe_2$ film marked by the A, B, and C, as shown in the inset STM image. For the three domains, the STS results are all dominated by a large electronic bandgap, and the domains have nearly the same band gap value. The valence band maximum (VBM) and conduction band minimum (CBM) are seen to be located at −1.25 and 0.61 eV, respectively. Therefore, our STS measurements yield a value for the electronic bandgap of single-layer $MoSe_2$/Au(111) of $E_g = E_{CBM} - E_{VBM}$ = 1.86 eV. In addition, although the three distinct domains have similar energy gaps, there is a remarkable difference among domains in the conduction band, which reflects the modulation effects of the moiré superstructure.[31] Furthermore, the DFT-calculated density of states (DOS), based on the optimized freestanding single-layer $MoSe_2$, is shown in the pink region in Figure 3a, which fits well with the experimental dI/dV results.

Considering the bulk structure of $MoSe_2$, there are two types of low-index edge terminations of a $MoSe_2$ hexagonal island: the $(10\bar{1}0)$ Mo edge and the $(\bar{1}010)$ Se edge. Due to the 6-fold symmetry of the $MoSe_2$ sheet, the exact shape of a $MoSe_2$ island is supposed to be a hexagon, shaped by two alternating types of edges, Se edges and Mo edges. When further considering the relative edge free energies of two different low-index edges in the equilibrium state, the single-layer $MoSe_2$ islands should prefer to expose the more stable edges, exhibiting a truncated hexagon with various lengths or even a triangle. In our case, many observed $MoSe_2$ islands have adopted a triangular shape, as illustrated in Figure 1a, indicating either of the two edges is preferable. According to previous work about MoS_2 clusters on the Au(111) system[27] and our

DOI: 10.1021/acsnano.6b07512
ACS Nano 2017, 11, 1689−1695

experimental condition of excess Se atoms, these triangular-shaped $MoSe_2$ islands are most likely to terminate with the $(10\bar{1}0)$ Mo edge, chemisorbing additional Se atoms to saturate the dangling bonds of exposed Mo atoms. However, a typical truncated hexagonal $MoSe_2$ island with three alternate longer edges and three alternate shorter edges was also observed in the inset STM image of Figure 3b, where possibly both Se edges and Mo edges coexisted. To identify the electronic structure differences of two typical edges, we performed STS characterizations on the edge of the truncated $MoSe_2$ island. Figure 3b presents six normalized dI/dV curves taken on the six edges of the $MoSe_2$ island (the inset STM image). Obviously, the STS results are classified into two groups, red group (three longer edges) and black group (three shorter edges). The main difference between the two groups is that the onset of the red group is earlier than that of the black group in positive sample bias.

Figure 4a shows an atomically resolved STM image of one edge, which presents regular arrays of rodlike protrusions.

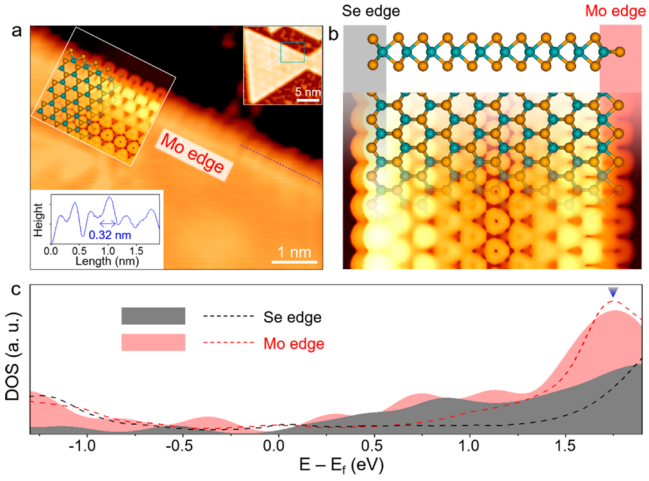

Figure 4. Edge visualization and edge states of the $MoSe_2$ island. (a) Atomically resolved STM image of Mo edge, which is a zoom-in image from the triangular $MoSe_2$ island in the upper right of (a). Inside the white frame is the atomic model of the Mo edge and related STM simulation. Lower left: height profile of Mo edge marked by a dashed blue line. (b) Side view (upper panel) and top view (middle panel) of the optimized configurations of $MoSe_2$ ribbon. Simulated STM image (down panel) is calculated on the basis of the ribbon model at a bias of −1.5 V. Se edge and Mo edge are marked by black and red backgrounds, respectively. (c) Theoretical PDOS and experimental dI/dV spectra of different edges of $MoSe_2$. The black and red shadows represent the calculated DOS projected on the marginal three atoms of the Se edge and the Mo edge in the model, respectively. The black and red dashed lines are the averaged experimental dI/dV curves for the two groups in Figure 3b. Scanning parameters: (a) V_s = −0.01 V, I_t = 4.0 nA.

According to the above discussions, this edge belongs to the red group mentioned above. The distance between two protrusions is about 3.2 Å according to the inset line profile. To obtain a further insight into the edge terminations of $MoSe_2$ islands, we performed the DFT calculations based on the $MoSe_2$ ribbon model (illustrated in the middle part of Figure 4b). We built a $1 \times 5\sqrt{3}$ $MoSe_2$ ribbon supercell terminated by two types of edges, where the left edge (marked by the black rectangle) is the bare Se edge and the right edge (marked by the red rectangle) is the Mo edge. Additionally, one more Se atom chemisorbs in between the exposed Mo atoms in the Mo edge, binding with two Mo atoms and lying in the plane of Mo atoms. (See more detailed analysis from the calculation results of $MoSe_2$ edges with different terminations in Figure S3, confirming that the Mo edge terminated with one more Se atom and the bare Se edge are energetically preferable.[32] Meanwhile, the width of the $MoSe_2$ ribbon has been checked far enough to isolate the edge states (Figure S4).) From the side view in the upper panel of Figure 4b, we find that structural deformation occurs at the Mo edge, whereas no deformation is obvious at the Se edge. Furthermore, the black and red shadows in Figure 4c represent the calculated DOS projected on the marginal three atoms of a Se edge and a Mo edge in the model, respectively. Except for some little peaks of the two curves around the Fermi level, which indicate the edge states of the ribbon, the key distinction is that in the unoccupied state, red shadows exhibit an earlier onset relative to the black curve, which fits well with the black and red dashed lines (the averaged experimental dI/dV curves for the two groups in Figure 3b). In order to demonstrate the edge states of the two edges more clearly, we carried out an STM simulation for the $MoSe_2$ ribbon. The lower panel in Figure 4b shows the simulated image, in which both the Se edge (left, black shadow) and the Mo edge (right, red shadow) look brighter than the middle of $MoSe_2$, *i.e.*, two one-dimensional (1D) edge states, which is consistent with experimental observations (Figure 1a and Figure 3b, where bright brims exist near the edge of $MoSe_2$ islands). Compared to MoS_2,[33] one-dimensional metallic edge states of $MoSe_2$ may result from the orbital hybridization between the Mo 3d state and Se 4p state. Meanwhile, Se edge looks brighter than that of the Mo edge, which is also fit the experimental results very well (Figure S5). (See Figure S6 for the simulated STM images of other edge configurations.)

In addition, we measured the distance between the two outermost Se atoms on the Mo edge in the model shown in Figure 4b (3.3 Å), which is close to the distance between two protrusions (3.2 Å), as mentioned with regard to Figure 4a. Meanwhile, as shown in the white frame in the inset of Figure 4a, the model of Mo edge saturated with single Se atoms and the corresponding simulated STM image are overlaid on the highly resolved STM image of $MoSe_2$ edge. Obviously, it fits quite well with the edge morphology in the STM image. The excellent agreement between the highly resolved STM image of $MoSe_2$ edge and the simulated image directly confirms that the selected edge (longer edge) of $MoSe_2$ islands is a Mo edge saturated with single Se atoms.

To investigate the origin of the electronic state differences of Se edges and Mo edges at positive sample bias, we calculated the projected DOS (PDOS) on the marginal Se and Mo atoms of the corresponding edges. Figure 5a,b show the PDOS for the Se and Mo atoms at the Se edge and Mo edge, which are marked by black and red circles in the inset, respectively. The shadows in the figures indicate the energy window, about 1.5–1.9 eV, in which the two types of edges exhibit different electron states, as shown in Figure 4c, and the blue triangles mark the exact energy value for the peak of Mo edge. For the Mo edge, in the marked energy window, the p_z orbital of Se atom and the d_{xz} orbital of Mo atom strongly couple, resulting in a prior peak of DOS in Figure 4c, whereas for the Se edge, no orbitals couple for Se and Mo atoms in the corresponding energy window. It can be concluded that different atomic configurations induce the distinction of chemical environment

DOI: 10.1021/acsnano.6b07512
ACS Nano 2017, 11, 1689–1695

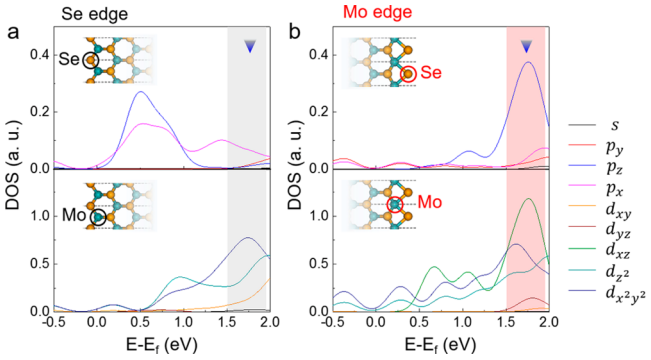

Figure 5. Calculated projected DOS (PDOS) on marginal Se and Mo atoms of corresponding edges. (a) For the Se edge, the PDOS of the marginal Se atom (upper panel, marked by the black circle in the inset model) and Mo atom (lower panel, marked by the black circle) are plotted. The gray rectangle marks the energy window of 1.5−1.9 eV. (b) For the Mo edge, the PDOS of the marginal Se atom (upper panel) and the Mo atom (lower panel), which are marked by red circles in insets, are plotted. Red rectangle marks the same range of energy window as in (a).

for marginal Se and Mo atoms on each type of edge and further influence the orbital couplings of corresponding atoms. The discussion above both explains what we measured in the STS spectra (Figure 4c) and exactly confirms our prediction that the longer edges of $MoSe_2$ islands are Mo edges with single Se atoms saturated and the shorter ones are the bare Se edges.

CONCLUSIONS

We have successfully synthesized high-quality, single-layer $MoSe_2$ islands with two types of edges epitaxially grown on Au(111) surfaces by MBE. By means of STM and LEED characterizations, we find that the single-layer $MoSe_2$ aligns with the direction of the Au substrate and shows a moiré superstructure with a 2.30 nm periodicity. DFT calculations identify that the edge terminations of the $MoSe_2$ islands are selenium monomer saturated Mo edges and bare Se edges. STS measurements of a single-layer $MoSe_2$ island show that the onset of localized electronic state in Mo edges is earlier than that in Se edges at positive sample bias. Meanwhile, DFT calculations confirm that the distinct differences in the electronic state for two edges result from the coupling between the p_z orbital of Se atoms and the d_{xz} orbital of Mo atoms for Mo edges, whereas there is no similar coupling for Se edges. This work can enrich the knowledge of the basic atomic structure and corresponding electronic properties of 2D materials' edges.

METHODS

Sample Preparation and *in Situ* Characterizations. MBE deposition of $MoSe_2$ was carried out in a commercial ultrahigh vacuum (UHV) LT-STM system (Omicron) with a base pressure greater than the 1×10^{-10} mbar range. The chamber is equipped with standard equipment for surface preparation and analysis. The atomically clean Au(111) (MaTecK) surfaces were obtained by cycles of argon-ion sputtering and annealing to 773 K, and the cleanliness of the surfaces was verified by STM scanning. The atomic beams of Se (99.99%, Sigma-Aldrich) and Mo (99.9%, Goodfellow) were generated from a standard Knudsen cell (Kentax) and a commercially available e-beam cell (Omicron), respectively, and the sequence was as follows: deposit Se first and the deposit Mo with the flux ratio of Mo to Se about 1:10 to avoid alloy formation of Mo and Au. Moreover, the substrate was kept at room temperature during the deposition process and postannealed to 750 K for 30 min. Such deposition and annealing processes constitute one growth cycle. To obtain a large area of single-layer $MoSe_2$ sample, the growth cycle was repeated several times. After the preparation, the sample was transferred to the LT-STM operating at 77 K. STM images were acquired in the constant-current mode by using an electrochemically etched tungsten tip, and all given voltages were applied to the sample with respect to the tip. Nanotec Electronica WSxM software[34] was used to process the STM images shown here. It should be mentioned that the synthesis chamber and low-T chamber are in the same equipment. The sample can be transferred freely under UHV conditions. What is more, the low energy electron diffraction (LEED) was performed in the adjacent UHV chamber for the $MoSe_2$ on Au(111) system to identify the superstructure macroscopically. Scanning tunneling spectroscopy (STS) was conducted by using a lock-in amplifier with a bias modulation of 0.5 mV at 973 Hz in another UHV-STM system (Unisoku) at a base temperature of 4.2 K.

XPS and Raman Measurements. XPS spectra were acquired *via* an ESCALAB 250 Xi XPS microscope using an Al K α X-ray source. Raman spectra were acquired by a Renishaw spectrometer at 532 nm with about 1 mW power.

Calculations. All calculations were performed using density functional theory (DFT) within the Perdew−Burke−Ernzerhof (PBE)[35] parametrization of generalized gradient approximation (GGA)[36] for electronic exchange-correlation interaction and projector-augmented wave (PAW) potentials[37] to describe the core electrons, as implemented in the Vienna *ab initio* simulation package (VASP).[38,39] The periodic $MoSe_2$/Au(111) growth model includes three layers of Au substrate and one layer of $MoSe_2$. Atoms were fully relaxed, except the bottom layer of the Au substrate, until the net force on every atom was less than 0.02 eV/Å. A vacuum slab of 15 Å is selected to avoid interactions between neighboring supercells. The energy cutoff of the plane-wave basis sets was 400 eV, and the k-points sampling was γ only. A dispersion correction of total energy (DFT-D2 method of Grimme)[40] was used to incorporate the van der Waals interaction between the sample and substrate. To describe the electronic structure of our models more exactly, all density of states (DOS) calculations were on the basis of the hybrid PBE0 functional method.[41]

ASSOCIATED CONTENT

Supporting Information

The Supporting Information is available free of charge on the ACS Publications website at DOI: 10.1021/acsnano.6b07512.

Additional STM images of Se clusters and high-coverage $MoSe_2$ images on the Au(111) surface, height profile of one $MoSe_2$ island, FFT analysis of an atomic resolved $MoSe_2$ island, DFT calculations for edge configurations and related stability of $MoSe_2$ ribbon, checking for ribbon width, and simulated STM images for other edge configurations (PDF)

AUTHOR INFORMATION

Corresponding Authors

*E-mail: sxdu@iphy.ac.cn.

*E-mail: xlin@ucas.ac.cn.

ORCID

Shi-Xuan Du: 0000-0001-9323-1307

Author Contributions

†J.C.L. and D.-L.B. contributed equally to this work.

Notes

The authors declare no competing financial interest.

ACKNOWLEDGMENTS

We thank Yu-Yang Zhang and Sokrates T. Pantelides for constructive suggestions. We acknowledge financial support

DOI: 10.1021/acsnano.6b07512
ACS Nano 2017, 11, 1689−1695

from the National Key Research & Development Projects of China (2016YFA0202300), the National Basic Research Program of China (2013CBA01600), the National Natural Science Foundation of China (Nos. 61390501, 61471337, and 51325204), the CAS Hundred Talents Program, and the National Supercomputing Center in Tianjin. A portion of the research was performed at the CAS Key Laboratory of Vacuum Physics.

REFERENCES

(1) Chhowalla, M.; Shin, H. S.; Eda, G.; Li, L.-J.; Loh, K. P.; Zhang, H. The Chemistry of Two-Dimensional Layered Transition Metal Dichalcogenide Nanosheets. *Nat. Chem.* **2013**, *5*, 263−275.

(2) Wang, Q. H.; Kalantar-Zadeh, K.; Kis, A.; Coleman, J. N.; Strano, M. S. Electronics and Optoelectronics of Two-Dimensional Transition Metal Dichalcogenides. *Nat. Nanotechnol.* **2012**, *7*, 699−712.

(3) Kuc, A.; Zibouche, N.; Heine, T. Influence of Quantum Confinement on the Electronic Structure of the Transition Metal Sulfide TS_2. *Phys. Rev. B: Condens. Matter Mater. Phys.* **2011**, *83*, No. 245213, DOI: 10.1103/PhysRevB.83.245213.

(4) Mak, K. F.; Lee, C.; Hone, J.; Shan, J.; Heinz, T. F. Atomically Thin MoS_2: a New Direct-Gap Semiconductor. *Phys. Rev. Lett.* **2010**, *105*, No. 136805.

(5) Wu, S.; Huang, C.; Aivazian, G.; Ross, J. S.; Cobden, D. H.; Xu, X. Vapor-Solid Growth of High Optical Quality MoS_2 Monolayers with Near-Unity Valley Polarization. *ACS Nano* **2013**, *7*, 2768−2772.

(6) Xu, X.; Yao, W.; Xiao, D.; Heinz, T. F. Spin and Pseudospins in Layered Transition Metal Dichalcogenides. *Nat. Phys.* **2014**, *10*, 343−350.

(7) Xiao, D.; Liu, G.-B.; Feng, W.; Xu, X.; Yao, W. Coupled Spin and Valley Physics in Monolayers of MoS_2 and Other Group-VI Dichalcogenides. *Phys. Rev. Lett.* **2012**, *108*, No. 196802.

(8) Tongay, S.; Zhou, J.; Ataca, C.; Lo, K.; Matthews, T. S.; Li, J.; Grossman, J. C.; Wu, J. Thermally Driven Crossover from Indirect toward Direct Bandgap in 2D Semiconductors: $MoSe_2$ *versus* MoS_2. *Nano Lett.* **2012**, *12*, 5576−5580.

(9) Loferski, J. J. Theoretical Considerations Governing the Choice of the Optimum Semiconductor for Photovoltaic Solar Energy Conversion. *J. Appl. Phys.* **1956**, *27*, 777−784.

(10) Zhang, Y.; Chang, T.-R.; Zhou, B.; Cui, Y.-T.; Yan, H.; Liu, Z.; Schmitt, F.; Lee, J.; Moore, R.; Chen, Y.; Lin, H.; Jeng, H.-T.; Mo, S.-K.; Hussain, Z.; Bansil, A.; Shen, Z.-X. Direct Observation of the Transition from Indirect to Direct Bandgap in Atomically Thin Epitaxial $MoSe_2$. *Nat. Nanotechnol.* **2014**, *9*, 111−115.

(11) Zhu, Z. Y.; Cheng, Y. C.; Schwingenschloegl, U. Giant Spin-Orbit-Induced Spin Splitting in Two-Dimensional Transition-Metal Dichalcogenide Semiconductors. *Phys. Rev. B: Condens. Matter Mater. Phys.* **2011**, *84*, No. 153402.

(12) Splendiani, A.; Sun, L.; Zhang, Y.; Li, T.; Kim, J.; Chim, C.-Y.; Galli, G.; Wang, F. Emerging Photoluminescence in Monolayer MoS_2. *Nano Lett.* **2010**, *10*, 1271−1275.

(13) Cao, T.; Wang, G.; Han, W.; Ye, H.; Zhu, C.; Shi, J.; Niu, Q.; Tan, P.; Wang, E.; Liu, B.; Feng, J. Valley-Selective Circular Dichroism of Monolayer Molybdenum Disulphide. *Nat. Commun.* **2012**, *3*, 887.

(14) Zeng, H.; Dai, J.; Yao, W.; Xiao, D.; Cui, X. Valley Polarization in MoS_2 Monolayers by Optical Pumping. *Nat. Nanotechnol.* **2012**, *7*, 490−493.

(15) Ugeda, M. M.; Bradley, A. J.; Shi, S. F.; da Jornada, F. H.; Zhang, Y.; Qiu, D. Y.; Ruan, W.; Mo, S. K.; Hussain, Z.; Shen, Z. X.; Wang, F.; Louie, S. G.; Crommie, M. F. Giant Bandgap Renormalization and Excitonic Effects in a Monolayer Transition Metal Dichalcogenide Semiconductor. *Nat. Mater.* **2014**, *13*, 1091−1095.

(16) Magda, G. Z.; Jin, X.; Hagymasi, I.; Vancso, P.; Osvath, Z.; Nemes-Incze, P.; Hwang, C.; Biro, L. P.; Tapaszto, L. Room-Temperature Magnetic Order on Zigzag Edges of Narrow Graphene Nanoribbons. *Nature* **2014**, *514*, 608−611.

(17) Prins, R.; Debeer, V. H. J.; Somorjai, G. A. Structure and Function of the Catalyst and the Promoter in Co-Mo Hydrodesulfurization Catalysts. *Catal. Rev.: Sci. Eng.* **1989**, *31*, 1−41.

(18) Ahmed, S. M.; Gerischer, H. Influence of Crystal-Surface Orientation on Redox Reactions at Semiconducting MoS_2. *Electrochim. Acta* **1979**, *24*, 705−711.

(19) Hinnemann, B.; Moses, P. G.; Bonde, J.; Jorgensen, K. P.; Nielsen, J. H.; Horch, S.; Chorkendorff, I.; Norskov, J. K. Biornimetic Hydrogen Evolution: MoS_2 Nanoparticles as Catalyst for Hydrogen Evolution. *J. Am. Chem. Soc.* **2005**, *127*, 5308−5309.

(20) Jaramillo, T. F.; Jorgensen, K. P.; Bonde, J.; Nielsen, J. H.; Horch, S.; Chorkendorff, I. Identification of Active Edge Sites for Electrochemical H-2 Evolution from MoS_2 Nanocatalysts. *Science* **2007**, *317*, 100−102.

(21) Karunadasa, H. I.; Montalvo, E.; Sun, Y.; Majda, M.; Long, J. R.; Chang, C. J. A Molecular MoS_2 Edge Site Mimic for Catalytic Hydrogen Generation. *Science* **2012**, *335*, 698−702.

(22) Lauritsen, J. V.; Bollinger, M. V.; Laegsgaard, E.; Jacobsen, K. W.; Norskov, J. K.; Clausen, B. S.; Topsoe, H.; Besenbacher, F. Atomic-Scale Insight into Structure and Morphology Changes of MoS_2 Nanoclusters in Hydrotreating Catalysts. *J. Catal.* **2004**, *221*, 510−522.

(23) Tsai, C.; Chan, K. R.; Abild-Pedersen, F.; Norskov, J. K. Active Edge Sites in $MoSe_2$ and WSe_2 Catalysts for the Hydrogen Evolution Reaction: a Density Functional Study. *Phys. Chem. Chem. Phys.* **2014**, *16*, 13156−13164.

(24) Sorensen, S. G.; Fuchtbauer, H. G.; Tuxen, A. K.; Walton, A. S.; Lauritsen, J. V. Structure and Electronic Properties of *in situ* Synthesized Single-Layer MoS_2 on a Gold Surface. *ACS Nano* **2014**, *8*, 6788−6796.

(25) Gronborg, S. S.; Ulstrup, S.; Bianchi, M.; Dendzik, M.; Sanders, C. E.; Lauritsen, J. V.; Hofmann, P.; Miwa, J. A. Synthesis of Epitaxial Single-Layer MoS_2 on Au(111). *Langmuir* **2015**, *31*, 9700−9706.

(26) Leavitt, A. J.; Beebe, T. P. Chemical-Reactivity Studies of Hydrogen-Sulfide On Au(111). *Surf. Sci.* **1994**, *314*, 23−33.

(27) Helveg, S.; Lauritsen, J. V.; Laegsgaard, E.; Stensgaard, I.; Norskov, J. K.; Clausen, B. S.; Topsoe, H.; Besenbacher, F. Atomic-Scale Structure of Single-Layer MoS_2 Nanoclusters. *Phys. Rev. Lett.* **2000**, *84*, 951−954.

(28) Abdallah, W. A.; Nelson, A. E. Characterization of $MoSe_2$(0001) and Ion-Sputtered $MoSe_2$ by XPS. *J. Mater. Sci.* **2005**, *40*, 2679−2681.

(29) Utama, M. I. B.; Lu, X.; Zhan, D.; Ha, S. T.; Yuan, Y.; Shen, Z.; Xiong, Q. Etching-Free Patterning Method for Electrical Characterization of Atomically Thin $MoSe_2$ Films Grown by Chemical Vapor Deposition. *Nanoscale* **2014**, *6*, 12376−12382.

(30) Lee, L. T. L.; He, J.; Wang, B.; Ma, Y.; Wong, K. Y.; Li, Q.; Xiao, X.; Chen, T. Few-Layer $MoSe_2$ Possessing High Catalytic Activity towards Lodide/Tri-iodide Redox Shuttles. *Sci. Rep.* **2014**, *4*, 4063.

(31) Voloshina, E. N.; Fertitta, E.; Garhofer, A.; Mittendorfer, F.; Fonin, M.; Thissen, A.; Dedkov, Y. S. Electronic Structure and Imaging Contrast of Graphene Moire on Metals. *Sci. Rep.* **2013**, *3*, 1072.

(32) Zan, W.; Hu, Z.; Zhang, Z.; Yakobson, B. I. Phase Crossover in Transition Metal Dichalcogenide Nanoclusters. *Nanoscale* **2016**, *8*, 19154−19160.

(33) Bollinger, M. V.; Lauritsen, J. V.; Jacobsen, K. W.; Norskov, J. K.; Helveg, S.; Besenbacher, F. One-Dimensional Metallic Edge States in MoS_2. *Phys. Rev. Lett.* **2001**, *87*, No. 196803.

(34) Horcas, I.; Fernandez, R.; Gomez-Rodriguez, J. M.; Colchero, J.; Gomez-Herrero, J.; Baro, A. M. WSXM: a Software for Scanning Probe Microscopy and a Tool for Nanotechnology. *Rev. Sci. Instrum.* **2007**, *78*, 013705.

(35) Perdew, J. P.; Burke, K.; Ernzerhof, M. Generalized Gradient Approximation Made Simple. *Phys. Rev. Lett.* **1996**, *77*, 3865−3868.

(36) Perdew, J. P.; Chevary, J. A.; Vosko, S. H.; Jackson, K. A.; Pederson, M. R.; Singh, D. J.; Fiolhais, C. Atoms, Molecules, Solids, and Surfaces: Applications of the Generalized Gradient Approximation for Exchange and Correlation. *Phys. Rev. B: Condens. Matter Mater. Phys.* **1992**, *46*, 6671−6687.

DOI: 10.1021/acsnano.6b07512
ACS Nano 2017, 11, 1689−1695

(37) Kresse, G.; Joubert, D. From Ultrasoft Pseudopotentials to the Projector Augmented-Wave Method. *Phys. Rev. B: Condens. Matter Mater. Phys.* **1999**, *59*, 1758−1775.
(38) Kresse, G.; Furthmuller, J. Efficient Iterative Schemes for *ab Initio* Total-Energy Calculations Using a Plane-Wave Basis Set. *Phys. Rev. B: Condens. Matter Mater. Phys.* **1996**, *54*, 11169−11186.
(39) Vanderbilt, D. Soft Self-Consistent Pseudopotentials in a Generalized Eigenvalue Formalism. *Phys. Rev. B: Condens. Matter Mater. Phys.* **1990**, *41*, 7892−7895.
(40) Bucko, T.; Hafner, J.; Lebegue, S.; Angyan, J. G. Improved Description of the Structure of Molecular and Layered Crystals: *ab Initio* DFT Calculations with van der Waals Corrections. *J. Phys. Chem. A* **2010**, *114*, 11814−11824.
(41) Paier, J.; Marsman, M.; Hummer, K.; Kresse, G.; Gerber, I. C.; Ángyán, J. G. Screened Hybrid Density Functionals Applied to Solids. *J. Chem. Phys.* **2006**, *124*, 154709.

DOI: 10.1021/acsnano.6b07512
ACS Nano 2017, 11, 1689−1695